

Combining plug-in devices for reconfigurable removal of trichloroethylene and heavy metal ion in aqueous solution: Application and biosafety of iron-iron sulfide and its composites

Bongseop Kwak^a, Jungwook Choi^{b,**}, Jiseok Lim^{b,***}, Jeong Hoon Byeon^{b,*}

^a College of Medicine, Dongguk University, Goyang 10326, Republic of Korea

^b School of Mechanical Engineering, Yeungnam University, Gyeongsan 38541, Republic of Korea

ARTICLE INFO

Handling Editor: Prof. Jiri Jaromir Klemes

Keywords:

Smart water treatment
Reconfigurable contaminant removal
Trichloroethylene
Heavy metal ion
Safe-by-design

ABSTRACT

The development of artificial intelligent (AI) planning for smart water treatment and the exploration of digitizable continuous-flow fabrication platform comprising electrically operable reactions for reconfigurable contaminant removal are two important challenges in future water purification technology. Most research and development efforts as well as the investment in water purifying materials have been focusing on the dimensions, compositions, or architectures containing highly adsorptive and catalytic components for effective combinatorial contaminant removal. However, limited attempts have been made to secure a digital system for adjusting the supply of existing adsorbents and chemicals to respond to transient or nonuniform distribution of contaminant load. To utilize AI planning in a more practical manner, developing a plug-in platform is necessary for reconfigurable fabrication that enables *in situ* supply of different water purifying materials. Therefore, a platform suitable for handling different material architectures was constructed by selecting different operation modes of plug-in reactionware (spark ablation, droplet generation, and photon supply) to modulate the architectures of water purifying materials. First, iron-iron sulfide (Fe-FeS) was fabricated using Fe nanoparticles and thiol vapors under photoirradiation, followed by combining the resulting Fe-FeS with metal (cobalt, nickel, or palladium) nanoparticles or graphene nanosheets to enhance the trichloroethylene (from 0.135 to 0.221 h⁻¹ in removal kinetics) or heavy metal ion (from 299 to 592 mg g⁻¹ in adsorption capacity) removal. Finally, *in vitro* toxicological analyses were conducted to determine biosafety of the resulting materials. The results of cell viability and reactive oxygen species profiles indicated that further investigation is required to realize the safe-by-design concept.

1. Introduction

Removal of organic and inorganic contaminants in water has been extensively investigated by employing various functional materials for adsorption, coagulation, oxidation, reduction, catalysis, and membrane filtration due to their advantageous physicochemical properties (Fan et al., 2018). Various types of nanoparticles (NPs) have been recently developed and applied as active components for the remediation of contaminated water. They are typically injected into the water to provide a function for contaminant removal (Wang et al., 2019). Chemical surface modification with NPs of fibrous media was also used for

enhancing contaminant removal in membrane filtration (Guo et al., 2017). Furthermore, multicomponent NPs for water purification have received considerable attention because of their combinatorial or synergistic effects resulting from the interactions between their components (Kim et al., 2011; Li et al., 2015; Santhosh et al., 2016; Zhang et al., 2016).

The typical protocols for hydrothermal syntheses of functional NPs for water purification involve multistep wet chemistry as well as manual pretreatments and posttreatments (Choudhury et al., 2018; Kim et al., 2011; Li et al., 2017; Mohamed et al., 2020). Toxic acids, bases, and templates, including surfactants are widely used to synthesize water

* Corresponding author.

** Corresponding author.

*** Corresponding author.

E-mail addresses: jwc@yu.ac.kr (J. Choi), jlim@yu.ac.kr (J. Lim), postjb@yu.ac.kr (J.H. Byeon).

<https://doi.org/10.1016/j.jclepro.2021.128069>

Received 15 March 2021; Received in revised form 1 June 2021; Accepted 21 June 2021

Available online 23 June 2021

0959-6526/© 2021 Elsevier Ltd. All rights reserved.

purifying materials with the desired physicochemical properties. These water purifying materials have exhibited unique and enhanced performance; however, toxicities or adverse health effects caused by the interactions between the purifying materials and biological matter represent challenges for their safe use (Jiang and Ladewig, 2020; Verma and Samanta, 2018; Xin-yan et al., 2019). Moreover, loading of additional functional compounds on the materials for enhancing their purification performance complicate their fabrication because they require further processes, which include complex controls (Kim et al., 2011; Wang et al., 2019). This implies that a low-emission simple process is essential for the fabrication of biosafe purifying materials to be used in practical water treatment processes.

A previous study used artificial intelligence (AI) planning to operate water purification (Aani et al., 2020; Ye et al., 2020); however, the study did not provide any specific insights related to plug-in water purification platforms that adapt to AI (Zhao et al., 2020). Most AI-based strategies mainly focus on minimizing the complexities and complications in water purification through big data exchanges, digital twins, or multivariate statistical approaches to optimize the operation conditions (Curl et al., 2019). Ensuring smart water purification based on AI still depends on manual works by expert plant engineers and material chemists, even though the advances in automated synthesis of functional organic compounds have reduced the manual processes (Coley et al., 2019). To utilize AI efficiently for smart water purification, specifically, made-to-apply water purifying materials in flow should be autonomously fabricated. Thus, these systems still require large investments and research efforts to validate their effectiveness, which limits the practical applications of smart strategies for water purification. Hence, an electrically operable and reconfigurable platform for *in situ* fabrication of water purifying materials with modifiable operation modes and functions is essential for successful incorporation of the AI technologies to develop smart water purification systems.

Therefore, in this study, an electrically operable platform was developed for the reconfigurable fabrication of Fe–FeS and its composites by single-pass assembly that could be adapted in continuous-flow processes (Hartrampf et al., 2020; Sui et al., 2020). The platform includes serial connection of plug-in reactionware (spark ablation, droplet generation, and photon supply; Figs. 1 and S1) under ambient nitrogen gas stream for built-to-order continuous supply of water purifying materials according to reconfigurable assembly of Fe-rich Fe–FeS, and hydrogenation metal nanocatalysts (M: Co, Ni, or Pd) or commercially available graphene (G) nanosheets. Nanoscale Fe–FeS, which is an alternative to nanoscale zero-valent iron (NZVI), was recently introduced to provide a stable removal of trichloroethylene (TCE), which is a toxic and persistent water contaminant (Elkin et al., 2020), as well as heavy metal ions (HM^+), which are non-biodegradable and chemically stable materials (Podgorski and Berg, 2020; Zhang et al., 2019), from water because of its enhanced electron transfer compared to NZVI. In addition, nanoscale Fe–FeS offers a high surface roughness that facilitates the adsorption of the contaminants (Chandrasekaran et al., 2019; Dong et al., 2019; Gong et al., 2016; Gu et al., 2017; Xu et al., 2020). Incorporating Co, Ni, or Pd NPs (catalyzing hydrogen generation) onto an Fe–FeS base was recently investigated to avoid the rapid corrosion of Fe–FeS, which enhances the dechlorination kinetics and stability of Fe–FeS during TCE removal compared to those of Fe–FeS alone (Kim et al., 2014). Selecting an appropriate metal catalyst to be incorporated onto Fe–FeS can enhance the removal and dechlorination of TCE (Kim et al., 2013); thus, in-line co-supply of the catalyst NPs with Fe–FeS may be useful to enhance the TCE removal in a built-to-order manner. In case of HM^+ removal, G nanosheets are known to be one of the effective additives that increases the adsorption capacity of Fe–FeS (Yin et al., 2020; Zhang et al., 2019). A self-assembly of Fe–FeS and G followed by their supply into HM^+ -containing aqueous solution in a single-pass configuration may also enhance the adsorption of HM^+ . Some functional or engineered materials were found to sometimes damage the human cells and tissues through physicochemical injury and generation

of reactive oxygen species (ROS) (He et al., 2020; Himly et al., 2020; Ma et al., 2014; Wang et al., 2017; Wu et al., 2020). Therefore, fundamental *in vitro* assays were further employed to determine cytotoxicities and oxidative stresses from the mammalian cell exposures to the resulting materials.

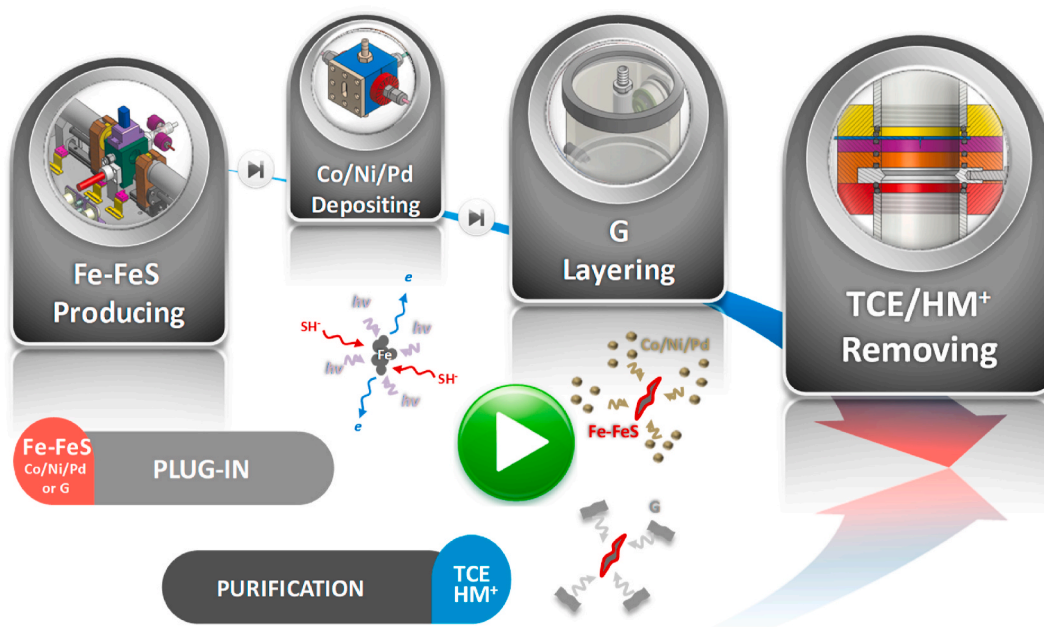
2. Experimental

2.1. Overall experimental procedure

Alternating current (AC) spark ablation (2.5 kV, 20 kHz) was used to generate continuous supply of Fe agglomerate NPs because it can produce NPs of various conductive materials through evaporation (ablating parts of the conductive materials), condensation (quenching vapors by a stream of ambient gas), and agglomeration (collisions between Fe singlet particles bipolarly charged by AC electric field) by switching on plug-in devices in the presence of ambient nitrogen gas stream (Gautam et al., 2019). In addition, thiol droplets were generated by a vibrating mesh nebulizer at a 128 kHz frequency (Thapa et al., 2018), and subsequently vaporized by the gas stream. The gas stream carried both Fe NPs and thiol vapors into a 185-nm ultraviolet (UV)-installed photo-chamber for their successive incorporation in the composite. This process started with the photoionization of the Fe NPs (Bian et al., 2020). The large work function (6.2 eV) of the photons produced by the UV irradiation facilitates the electron ejection from the surfaces of the Fe NPs, generating positive charges on the NPs that electrostatically interacted with the negatively charged groups of the peripheral thiol vapors in a diffusion dryer to construct FeS layers on the NPs (Fe–FeS) (Fig. S1). As shown in Fig. 1, further incorporation of M (Co, Ni, or Pd) NPs on the Fe–FeS was achieved by directly passing the Fe–FeS-laden gas stream through direct current (DC) spark ablation (3 kV, 1 kHz) chamber, where M NPs were deposited on the Fe–FeS mainly by Brownian collisions under the action of the DC spark because of the significantly larger diffusion coefficients of the NPs ($>10^3$) in the gas phase compared to those in the aqueous phase (Feng et al., 2015), resulting in the formation of Fe–FeS@M. Fe–FeS@G was also constructed via self-assembly of the Fe–FeS and G nanosheets, where the Fe–FeS-laden flow passed over an orifice of collision-type atomizer filled with G dispersed to form hybrid droplets. These droplets were then passed through another diffusion dryer for removing the solvent from the droplets to facilitate interaction between the Fe–FeS and G nanosheets to form composites (Byeon, 2016). The resulting Fe–FeS or one its composites (Fe–FeS@M and Fe–FeS@G) was eventually dispersed in an aqueous solution (containing a fixed amount of TCE or HM^+), and the solution was subsequently injected into a flow reactor with a polytetrafluoroethylene (PTFE) membrane filter to examine the purifying performance for 9 h. To determine biosafety of the resulting materials, 3-(4,5-dimethylthiazole-2-yl)-2,5-diphenyltetrazolium bromide (MTT) and dichloro-dihydro-fluorescein diacetate (DCFH-DA) assays were conducted to determine cell viability and the possibility of ROS generation, respectively. These assays were conducted after exposing to human dermal fibroblast (HDF, simulating dermal exposure) and bronchial epithelial (BEAS-2B, simulating inhalation exposure) cells to nanoscale Fe–FeS and their composites for 48 h.

2.2. Plug-in fabrication

Fe NPs were continuously produced via spark ablation (2.5 kV, 20 kHz) under ambient nitrogen gas flow (99.9999% purity) (1.5 L min^{-1}) by turning on an AC power supply (BPI-2K, Best Power, Korea) and mass flow controller (KOFLOC, Japan) in a single-pass configuration. An x-axis single-stage system (CSI Tech, Korea) was included into the spark ablation for automatically maintaining the spacing (1 mm) between the Fe rods during the ablation. As shown in Fig. S1, high temperature ($>5000 \text{ K}$) spark microchannels were formed between two identical Fe rods (3 mm diameter; FE-222564, Nilaco, Japan), which enabled the



evaporation of parts of the rods. The Fe vapors then condensed into singlet Fe particles through quenching by ambient nitrogen gas flow, and the particles were then agglomerated by electrostatic collision between the bipolarly charged particles from the AC electric field. These agglomerate NPs passed through a 185-nm UV (UVP, UK)-installed photochamber with thiol vapors generated by vibrating mesh nebulization (Pro-X, Aerogen, Ireland) located right after the spark ablation. Electron ejection from the UV (photon energy = 6.2 eV)-exposed singlet Fe particles (work function = 4.5 eV) during their passage through the photochamber formed positive charges on the Fe surfaces, which facilitate the electrostatic conjugation between the positively charged particles and the negatively charged thiol groups to form an Fe-S configuration. The fabrication of powder Fe-FeS suspended in nitrogen gas was completed by solvent extraction of Fe-FeS from the thiol droplets followed by passing it through a diffusion dryer. Different ratios (10:1 to 90:1) between Fe and S were achieved by modulating the concentration of 1-hexanethiol (Sigma-Aldrich, USA) in ethanol (10^{-3} to 10^{-1} v/v%) to generate thiol vapors. The Fe-FeS was harvested, dispersed in simulated contaminated water (TCE or HM^+ included), and precisely injected into a membrane filter (11807-47-N, Sartorius, Germany)-installed flow reactor to use as an active material for the removal of TCE or HM^+ .

Fe-FeS@G nanocomposites in the removal of TCE or HM^+ was compared to that of the base Fe-FeS to assess the reconfigurable operation.

2.3. Size distribution and surface charge

To examine the efficiency of the integration between spark-produced Fe NPs and vibrating nozzle-generated thiol vapors, in-flight size distributions of Fe, individual Fe NPs, and the thiol co-injected configuration (i.e., Fe–FeS) were obtained using a scanning mobility particle sizer (SMPS; 3936, TSI, USA) for 180 s. The dynamic light scattering (DLS) size distributions of Fe–FeS and individual Fe were also measured using a zetasizer (Nano ZS90, Malvern Instruments, UK) after the dispersion of the resulting particles in deionized water. The surface charges of Fe and Fe–FeS suspended in gaseous and aqueous media were obtained using an aerosol electrometer (Charme®, Palas, Germany) and a zetasizer equipped with an automatic titrator (MPT-2, Malvern Instruments, UK), respectively. Size classification of singlet Fe particles was determined using a nano differential mobility analyzer (NDMA; 3085, TSI, USA) to obtain average charges per particle.

2.4. Morphology

The morphologies of Fe, Fe–FeS Fe–FeS@M, and Fe–FeS@G were observed using transmission electron microscope (TEM; Tecnai G² F20 S-TWIN, FEI, USA) and scanning electron microscope (SEM; S-4800, Hitachi, Japan) after the direct deposition of the particles on carbon-coated copper grids (Tedpella, USA) through electrostatic precipitation (NPC-10, HCT, Korea).

2.5. Surface, optical, magnetic, and textural properties

The composition and hydrophobicity of Fe–FeS were obtained using energy-dispersive X-ray spectroscopy (EDX; S-4800, Hitachi, Japan) and contact angle goniometer (250, Ramé-Hart Instrument, USA), respectively. X-ray photoelectron (XPS; Axis-HIS, Kratos Analytical, Japan),

Raman, UV–Vis (T60, PG Instruments, UK), Fourier transform infrared (FTIR; iS-10, Thermo Electron, USA), and X-ray diffractometer (XRD; X'Pert³ MRD, Panalytical, UK) spectra of Fe and Fe–FeS were obtained to compare between them for confirming the sulfidation of Fe NPs. The magnetic properties of the Fe and Fe–FeS particles were also compared using a vibrating sample magnetometer (VSM; 7404, Lake Shore Cryotronics, USA) to examine the relative magnetic reactivities. The textural properties of Fe–FeS and Fe–FeS@G were analyzed using a porosimeter (ASAP, 2010; Micromeritics, USA) to study the specific surface areas and pore volumes in relation to the adsorption-desorption isotherms and pore size distributions.

2.6. TCE and HM⁺ removal

To determine the removal and dechlorination efficiencies of TCE, a gas chromatography-flame ionization detection (GC-FID; 6980 N, Agilent, USA) containing a capillary column (DB-624, Agilent, USA) and UV–Vis spectrophotometer (UV-2450, Shimadzu, Japan) were simultaneously employed to measure the concentrations of TCE and chlorine ion, respectively. In the GC-FID, the reacted solution was periodically sampled from the PTFE membrane filter (11807, Sartorius, Germany)-installed flow reactor, followed by the extraction of TCE using pure n-hexane. For assessing the HM⁺ adsorption capacities, the reacted solution was collected to measure the residual concentrations of lead, mercury, cadmium, or arsenic aqueous ions using inductively coupled plasma-optical emission spectrometry (ICP-OES; OPTIMA 8300, PerkinElmer, USA).

2.7. Cytotoxicity

In vitro cytotoxicities of Fe–FeS and its nanocomposites (Fe–FeS@Co, Fe–FeS@Ni, Fe–FeS@Pd, and Fe–FeS@G), in addition to individual Co, Ni, Pd, and G, were examined in HDF and BEAS-2B cells using MTT assay. Cells (2×10^4) dispersed in Dulbecco's Modified Eagle's medium (DMEM) were seeded in 96-well plates (Becton Dickinson Labware, USA) and incubated overnight at 37 °C. The cells were then exposed to the samples ($50\text{--}200 \mu\text{g mL}^{-1}$) for 48 h. After washing with phosphate buffered saline (PBS), MTT reagent (1.25 mg mL^{-1} in DMEM, $100 \mu\text{L}$) was added to each well. After a 3-h incubation in the dark, the cells were lysed. Next, the formazan crystals formed by viable cells were dissolved using dimethyl sulfoxide ($100 \mu\text{L}$). The absorbance of formazan was measured at 570 nm using a microplate reader (Multiskan EX, Thermo Scientific, USA) to estimate the cell viabilities.

2.8. ROS generation

Viable HDF or BEAS-2B cells were seeded in a 6-well plate (2×10^5

cells). After a 24-h incubation, the cells were exposed to the samples ($100 \mu\text{g mL}^{-1}$) and incubated for 6 h. The cells were then extracted, washed with PBS, and stained with DCFH-DA ($10 \mu\text{M}$) in media for 30 min in the dark. The fluorescence of intracellular DCF was then analyzed using flow cytometry.

3. Results and discussion

3.1. Fe NP generation and photoionization

The local high temperatures (several thousand Kelvins) provided by spark microchannels between the Fe rods resulted in vaporizing parts of the rods (Feng et al., 2016), which was followed by condensation of the vapors into singlet Fe particles through quenching by ambient nitrogen gas flow. The Fe particles were bipolarly charged due to the AC electric field used during spark ablation, which results in the formation of agglomerate NPs (Fig. 2A) through electrostatic attraction between the positively and negatively charged singlet particles ($\sim 6 \text{ nm}$, by measuring hundreds of singlet particles). The resulting electric current of the bipolarly charged NPs was measured using an aerosol electrometer to be $0.0 \pm 4.2 \text{ fA}$ (nearly neutral in total), suggesting that the sparking frequency adopted to the ablation can generate equivalently bipolar charges, which cause quantitative agglomeration. The representative high-magnification TEM image and selected area electron diffraction (SAED) pattern exhibited Miller indices of (110) and (200) for body-centered cubic (bcc) Fe, implying that the spark ablation is a suitable approach to supply precursor Fe NPs for further processing (Egeberg et al., 2019; Herman et al., 2011). An EDX was used in conjunction with SEM. The result of this analysis further confirmed the formation of agglomerate Fe NPs. Fig. 2B shows the α (Poudel et al., 2018) and q_{max} (Byeon and Roberts, 2014) as representative parameters for conferring in-flight conjugation activity with thiol to form FeS layers. A maximum of four elementary charges were generated on singlet Fe particles by photoionization (~ 0.7 photoionization rate) for 6.4 s. The mean charges (q_{mean}) per a singlet Fe particle (particle size was measured using a NDMA to be 6 nm) estimated using an aerosol electrometer to be $+0.8 \pm 0.25$ per particle based on the following formula: $q_{\text{mean}} = I_A/C_N Qe$, where I_A , C_N , Q , and e are the aerosol current, aerosol number concentration, sampling flow rate, and elementary charge ($1.6 \times 10^{-19} \text{ C}$), respectively. This implies that photoionization can generate the positive charges required for the electrostatic reaction with the negatively charged thiol, even if recombination occurs between the positively charged Fe surface and the ejected electrons.

3.2. Fe–FeS formation

To examine the transformation of the photoionized Fe to Fe–FeS, in-

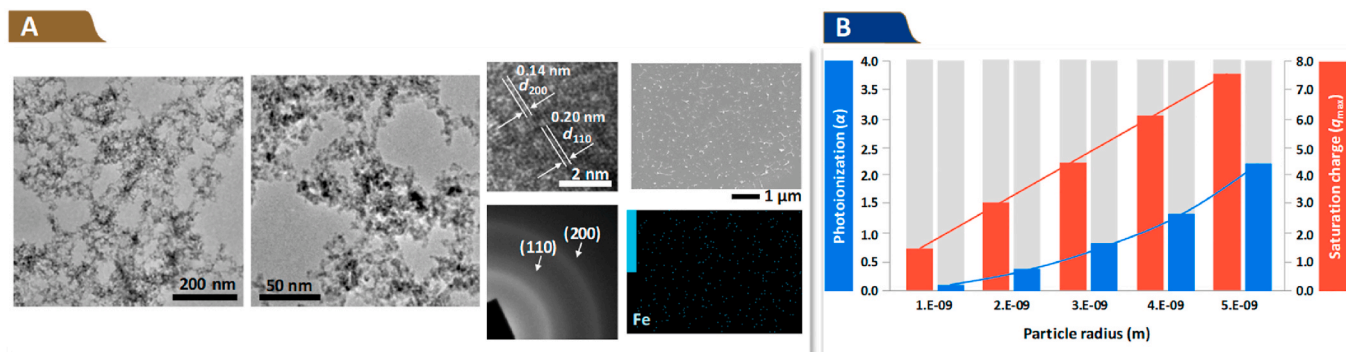


Fig. 2. The plug-in manufacturing and subsequent photoionization of Fe agglomerate NPs. (A) Low- and high-magnification TEM images, including a representative SAED pattern, SEM image, and EDX map. The NPs from spark ablation were directly collected on carbon-coated copper grids using an aerosol impactor sampler. (B) Theoretical photoionization rate (α) and saturation surface charge (q_{max}) as a function of singlet particle diameter under a 185-nm UV (light photon energy = 6.2 eV) exposure to the Fe NPs (work function = 4.5 eV).

flight size distributions of the Fe NPs with thiol vapors were obtained in the absence and presence of photoirradiation using a SMPS. The data representing the size distribution of the Fe NPs, such as geometric mean diameter (GMD), geometric standard deviation (GSD), and total number concentration (TNC), were found to shift to a larger and broader configuration after passing through the photochamber and diffusion dryer (Fig. S2A). No peaks representing Fe–FeS were observed, which suggests that nearly all Fe NPs transformed to different constructs because of photoionization. This transformation was further investigated via DLS measurements after two samples of Fe and Fe–FeS were dispersed in deionized water (Fig. S2B). A significant change in the size distribution (mean diameter [MD] = 73.8–174.0 nm) was observed during DLS. However, only slight differences in the size distribution were caused by the difference in particle dynamics in different media as well as the difference in the measuring principles of SMPS and DLS. In addition, the pH-zeta potential profiles of Fe and Fe–FeS exhibited different isoelectric points at 7.1 and 3.7, respectively (Fig. S2C), which confirms that the negatively charged S-containing groups were incorporated with the Fe NPs during the plug-in single-pass reaction.

To confirm the transformation of Fe to Fe–FeS based on morphological changes. The resulting particles were collected on a carbon-coated copper grid and observed using SEM. Fig. 3A–3C shows low- and high-magnification SEM images of the resulting particles that exhibit several bundles consisted of entangled short rods (200–300 nm in length), which are comparable to the nanoscale Fe–FeS reported in previous studies (Cao et al., 2017; Zhang et al., 2018). The representative TEM images (Fig. 3D and E) confirmed the entangled architecture, and the high-magnification image for the surface and core regions mainly exhibited interplanar distances, where 0.26/0.29 and 0.14 nm corresponded to (101)/(100) for hexagonal FeS (Wang et al., 2015) and (200) for bcc Fe microstructures, respectively. The formation of this Fe–FeS “core-shell” architecture may be attributed to non-stoichiometric supply of thiols as well as the limited or negligible deep self-diffusion of incoming S-containing groups into the core region of the agglomerate Fe

NPs when passing through the preformed FeS outermost layers (diffusion coefficient of S [D_S] = 1.75×10^{-14} exp [−132100/RT], where R and T are the gas constant and temperature, respectively) (Cummins et al., 2013). Similarly, the diffusion of Fe atoms into the surface was found to be negligible under ambient conditions. An EDX spectrum (Fig. 3F) of the resulting Fe–FeS clearly indicates characteristic S bands, and the dot distributions of elemental Fe and S coincided with the resulting particles (Fig. S3A), proving the formation of FeS layers from the in-flight incorporation of S with Fe during the transformation of agglomerate Fe NPs to the entangled short rods. Thus, larger hydrophobic surfaces were obtained compared to those of Fe NPs, which provide greater interaction with hydrophobic solutes in aqueous solution (Fig. S3B) (Xu et al., 2020).

Surface states of the resulting Fe–FeS were further determined through XPS, Raman, UV–visible (UV–Vis), and FTIR spectroscopies. The Fe 2p core level XPS spectra of the Fe and Fe–FeS (Fig. S3C) at 706 (Fe 2p_{3/2})–718 (Fe 2p_{1/2}) eV and 710 (Fe 2p_{3/2})–721 (Fe 2p_{1/2}) eV were attributed to the atomic (Fe⁰) and oxidized (Fe²⁺/Fe³⁺) Fe species, respectively (Dong et al., 2019). The Fe–FeS exhibited weaker Fe⁰ bands compared to Fe alone, while there were also shifts in the binding energy to higher energies in case of Fe–FeS, demonstrating the formation of Fe–S bindings (Su et al., 2018). In case of S 2p, the bands at 161–166 eV represented S^{2−} and SH[−] (Ren et al., 2019; Wu et al., 2018), and the band at 167–172 eV matched surficial sulfenylation (Fe–S–O–H) probably due to the coexistence of hydroxyl groups (from ethanol used for diluting thiol) with thiols (Parvez et al., 2018). This indicates that the designed plug-in reaction also generates the outermost functional groups (–SH and –SOH), which affects the surface charges (Fig. S2C). Fig. S3D shows the bands at 202 and 294 cm^{−1} obtained from a Fe–FeS-deposited glass disc (inset) that match the characteristic Raman vibrations of FeS (Niu et al., 2019) and another band around 380 cm^{−1} that can be attributed to the A_{1g} mode of the S sublattice for Fe-rich FeS structure (Genchev and Erbe, 2016). This further validates the plug-in reaction for the transformation of Fe (exhibiting no distinct

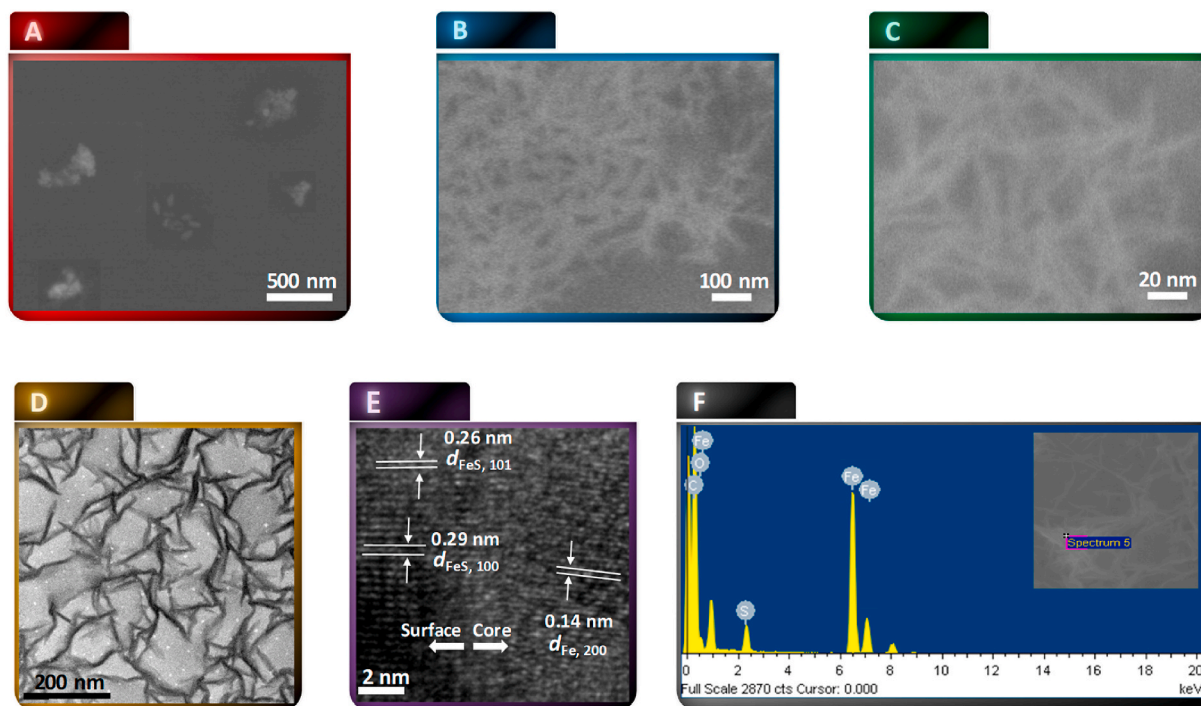


Fig. 3. Morphological and compositional analyses of the particles resulting from the photoionization of Fe NPs with thiol vapors. (A–C) Low- and high-magnification SEM images. The particles after photoionization and subsequent in-flight exposure to thiol vapors were directly collected on carbon-coated copper grids using an electrostatic aerosol sampler. (D, E) Low- and high-magnification TEM images of the resulting particles collected on the grids. (F) A representative EDX spectrum of the resulting particles on the grid (inset SEM image).

characteristic Raman bands) to FeS. The formation of FeS was also confirmed by the generation of UV–Vis absorption band between 400 and 550 nm compared to the spectrum of the Fe NPs (Fig. S3E) that matches the spectra reported in previous studies (Dutta et al., 2012; Maji et al., 2012). The spectral comparison in FTIR (Fig. S3F) indicated the existence of –SH (1740 cm^{-1}) and –SOH ($3300\text{--}2700\text{ cm}^{-1}$), matching the S 2p XPS spectra (Fig. S3C) (Poudel et al., 2019), which suggests that the plug-in platform is suitable to generate different surficial functional groups during metal sulfidation by modulating the composition of the peripheral vapors on metal surfaces.

For further characterizing the resulting Fe–FeS, VSM and XRD were used to compare bulk magnetic and crystalline properties, respectively, of Fe NPs in the absence and presence (under photoirradiation) of thiol vapors. Fig. S4A illustrates the differences in saturation magnetization at room temperature between the Fe (130 emu g^{-1}) and Fe–FeS (80 emu g^{-1}). It showed that both Fe and Fe–FeS exhibited magnetic reactivity even in low applied fields (inset). The decreases in magnetization and coercivity after the formation of FeS layers may be attributed to the exchange coupling effects between Fe and FeS microstructures, which is in agreement with the phenomena introduced in previous reports (Kim et al., 2011; Lv et al., 2018). Nonetheless, this characterization suggests that Fe-rich FeS produced by the plug-in reaction can easily retain detectable magnetic reactivities even with microstructural reconfiguration. The corresponding XRD profiles demonstrated that the higher peaks reflected distinct (110) and (200) Fe crystalline phases, whereas, the detected weak bands are assigned to Fe-rich FeS (Lv et al., 2018; Soori et al., 2016). No FeO_x bands were observed in the Fe–FeS spectrum, implying that the sulfenyl groups detected in XPS and FTIR analyses are only distributed on the outermost layers of Fe–FeS, probably due to the negligible self-diffusion of coexisting O atoms while passing through the preformed outermost FeS layers (Cummins et al., 2013). Regarding the transformation based on the comparative characterizations between the Fe and Fe–FeS, it can be suggested that the peripheral thiol vapors are first electrostatically incorporated to form Fe–S conjugates under photoirradiation (Fig. 4). Thus, the conjugated S atoms diffuse only into the outermost layers of the Fe NPs because of the restricted self-diffusion, where the surficial solid Fe^{2+} combines with S^{2-} to form FeS layers, resulting in the restructuring of the agglomerates into the entangled short rods. The formation of FeS was randomly oriented due to lattice mismatch with the agglomerated Fe backbone, resulting in the dominant growth of the (101) and (100) directions to form the entangled architectures along with the alignment defects. The H and OH groups linked to the S atoms generated surficial FeS–H and

FeS–OH layers that determine the electrostatic surface states of the resulting Fe–FeS.

3.3. TCE removal using Fe–FeS and Fe–FeS@M

The effectiveness of the developed plug-in platform was identified by testing the removal and dechlorination performance of the resulting Fe–FeS. The operation mode of the plug-in platform was reconfigured to find out the optimal mass ratio between Fe and S. This was specifically achieved by modulating the thiol content in the precursor solution, in which five ratios (10:1 to 90:1) were used for comparison between them, as well as with Fe NPs. The results (Fig. 5A) indicated that the formation of FeS enhanced the performance of both removal and dechlorination regardless of the Fe:S ratio compared to Fe NPs, which may be due to reduced corrosion rate (resulting from the more hydrophobic surface) and electron transfer resistance (resulting from the blockage of atomic H adsorption sites) (Fan et al., 2016; Xu et al., 2020). The differences in the kinetics between the removal and dechlorination reflected the removal results of both adsorption and dechlorination in all testing cases, including that using Fe NPs. Fig. 5B showed that the removal kinetics depended on the pH conditions because the –SH and –SOH groups on the surface of the resulting Fe–FeS may undergo protonation or deprotonation reactions in aqueous solution with the changes in the pH (Kim et al., 2013). Thus, this induced different reactivities of the Fe–FeS, in which increasing the pH generated higher TCE removal kinetics because of the increased deprotonated ligands at higher pH levels that promote the electron donation during dechlorination (Dong et al., 2018). These parametric studies for rationalizing the TCE removal at different Fe:S ratios or pH levels were concluded by operating electrically adaptive feeding devices for adjusting the thiol content or the acid/base balance, respectively, without any manual tasks. Utilizing this plug-in strategy will enable the fabrication and application of Fe–FeS to automatically reconfigure water purification systems based on AI without significantly involving the plant engineers and material chemists.

The modularity in the TCE removal was determined by directly depositing M (Co, Ni, or Pd) NPs onto preformed Fe–FeS, in which the deposition was conducted in in-flight single-pass process. Morphologies and microstructures of the M NPs were observed using TEM. As shown in Fig. S5A, the resulting M NPs exhibited agglomerate architectures. The figure also shows the SAED patterns, in which for the following Miller indices: (111), (200), (220), and (311) of singlet Co (4.6 nm), Ni (4.4 nm), and Pd (4.9 nm) particles are visible. This indicated that another spark ablation is required for additional supply of crystalline singlet Co,

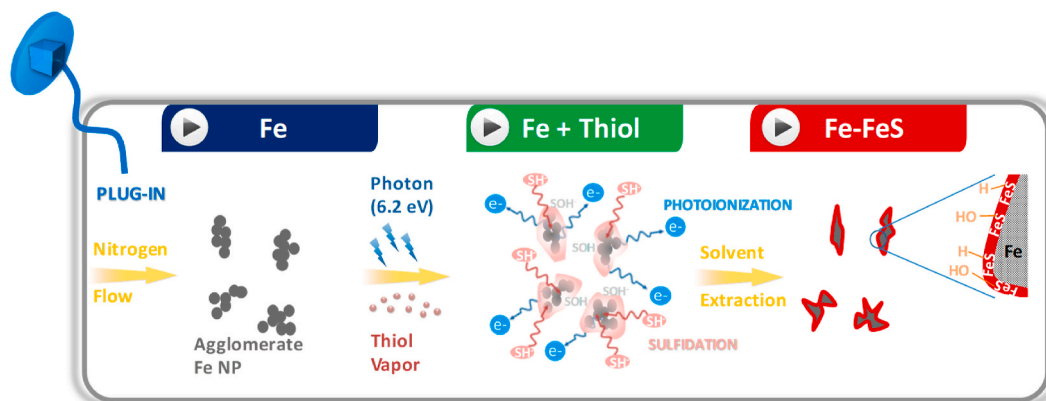


Fig. 4. Illustration of the in-flight Fe transformation into Fe–FeS by co-passage of Fe NPs and thiol vapors through the photochamber. Fe vapors from AC spark ablation of Fe rods were condensed into bipolarly charged singlet particles by ambient nitrogen gas flow. The particles were electrostatically gathered in the form of agglomerate (refer to Fig. 2A) under the AC electric field used for spark ablation. The exposure of the Fe agglomerate NPs with peripheral thiol vapors to a 185-nm UV light induced positive charges on the NPs (refer to Fig. 2B) that electrostatically combine with negatively charged groups of thiol to form FeS layers on the surface of the NPs. After passing through a diffusion dryer to extract the unreacted vapors, Fe–FeS was ready for injection into the simulated contaminated water or a DC spark chamber (or a collision-type atomizer) for further incorporation with M NPs (or G nanosheets).

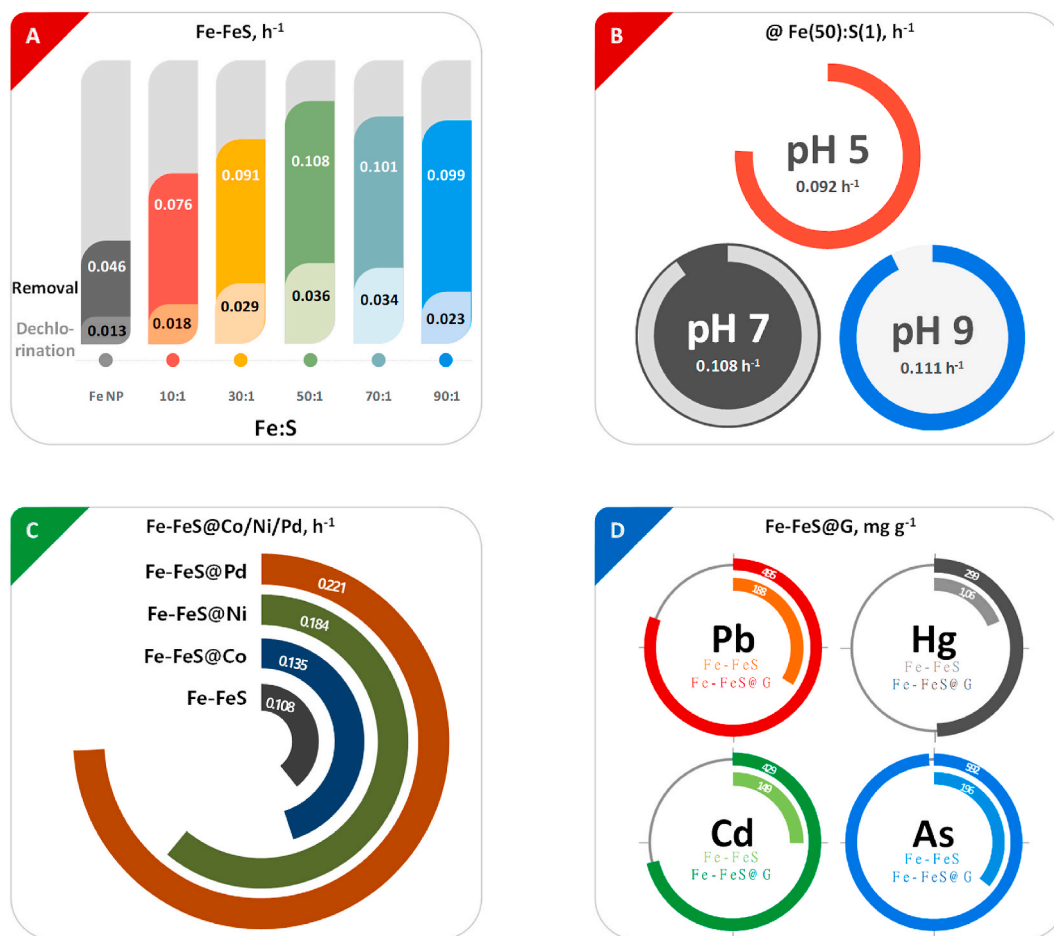


Fig. 5. TCE removal kinetics and HM⁺ adsorption capacity of Fe-FeS and its composites. The concentrations of both TCE and HM⁺ were 30 mg L⁻¹, and the Fe-FeS and its composites were dispersed for TCE and HM⁺ removal at concentrations of 5 g L⁻¹ and 0.5 g L⁻¹, respectively. The kinetics was assessed based on a 9 h operation period. (A) TCE removal (intense) and dichlorination (pale) kinetics of Fe-FeS as a function of Fe:S mass ratio. (B) TCE removal kinetics of Fe-FeS (Fe:S = 50:1) as a function of pH. (C) TCE removal kinetics of Fe-FeS@Co, Fe-FeS@Ni, and Fe-FeS@Pd, including base Fe-FeS (Fe:S = 50:1). The mass ratio between Fe and M (Co, Ni, or Pd) was found to be 9:1. (D) HM⁺ adsorption capacity of Fe-FeS@G, including base Fe-FeS (Fe:S = 20:1). The mass ratio between Fe and G was 76:24.

Ni, and Pd particles, but diffusional behaviors of ultrasmall (<5 nm) particles in gas phase were still strong for Brownian agglomeration even under the DC electric field (i.e., generating unipolar charges). In order to uniformly deposit the M NPs on the Fe-FeS base, the flow containing Fe-FeS and M NP passed over a nozzle (diameter = 0.5 mm) at the exit of the spark chamber to redistribute the agglomerated M NPs into singlet particles as a result of the pressure difference (before and after the nozzle)-induced shattering of the M NPs (Byeon, 2016). The representative SEM and TEM images (Fig. S5B) of the particles after the deposition of M NPs onto the Fe-FeS exhibited analogous architectures to the base Fe-FeS with no satellite agglomerates. The supplied M NPs can be observed in the high-magnification TEM as singlet particles on the surfaces of the Fe-FeS base. This implies that the fluidic oscillation at the nozzle can scatter the agglomerates on the Fe-FeS to form Fe-FeS@Co, Fe-FeS@Ni, or Fe-FeS@Pd nanocomposites. In addition, the unipolar charges (i.e., generating repulsive forces) on the agglomerates caused by the DC electric field used for the ablation might result in weak bindings between the singlet particles before entering the nozzle. Moreover, compositional analyses of the nanocomposites using EDX (Table S1) indicate that the mass ratios between Fe and M were found to be approximately 9:1. The slight differences in the mass fraction among Co, Ni, and Pd (Ni < Co < Pd) may be attributed to the difference in the ionization potentials (electron affinities: Co: 7.881 eV, Ni: 7.639 eV, and Pd: 8.337 eV) (Neogrady et al., 1997), which affect the production rates of zero-valent M atoms that were being condensed into M particles near

the spark microchannels. Fig. 5C shows a comparison between the TCE removal kinetics using the Fe-FeS@M nanocomposites, including base Fe-FeS. The diagram indicated that the M NPs clearly enhances the performance of base Fe-FeS. This enhancement may be attributed to the generation of active forms of hydrogen on the Co, Ni, or Pd particles that promote the electron transfer on the Fe-FeS (Kim et al., 2014; Xu et al., 2013). The differences in removal kinetics between the nanocomposites were likely due to the different electronic properties and surface atomic structures of the M NPs (Zhang et al., 1998). These results suggest that the plug-in modulation by the single-pass incorporation between base Fe-FeS and M may provide conceptual insights for its extending use in automated TCE removal by reconfiguring correlation between the Fe-FeS hybridization and the TCE removal kinetics.

3.4. HM⁺ removal using Fe-FeS and Fe-FeS@G

For modulating the HM⁺ removal, a commercially available G dispersion-filled collision-type atomizer and another diffusion dryer were serially connected to the Fe-FeS-laden gas stream to obtain Fe-FeS@G nanocomposites, taking into consideration of a previous report that introduced a significant enhancement in HM⁺ adsorption (Mahto et al., 2018). A representative TEM image (Fig. S5C) of the graphene sheets showed the flakes (lateral dimension = 100–400 nm) that were directly collected on a grid after the atomization and subsequent diffusion drying. The corresponding SAED pattern exhibited (001)

and (002) planes (Lee and Kang, 2016), proving the existence of graphitic layers in the flakes. Fig. S5D shows a SEM image of the nanocomposite after incorporating the graphene into Fe–FeS, in which the entangled architectures were clear compared to Fe–FeS alone. This morphological change was due to the interconnection between the Fe–FeS and G (low-magnification TEM image in Fig. S5D) (Zhao et al., 2017) during water extraction in the diffusion dryer, in which both the lattice fringes of FeS and G can be observed (high-magnification TEM image), indicating the presence of G layers on Fe–FeS. Compositional analysis of this nanocomposite presented readable fractions of C with Fe and S (Table S1), further proving the incorporation of G into Fe–FeS. The relatively greater fraction of elemental O in the Fe–FeS@G compared to other nanocomposites can be attributed to the O atoms in the G nanosheets. Before using Fe–FeS@G for HM^+ removal, an analogous approach involving Fe–FeS (Fig. 5A) was used to select the optimal Fe:S ratio for adsorption of aqueous HM^+ . The optimal mass fraction was found to be 20 (Fe):1 (S) that was universally used for the adsorption of

HM^+ (Pb^{2+} , Hg^{2+} , Cd^{2+} , and As^{3+}) in this study. Dispersing the Fe–FeS in the HM^+ -containing solution resulted in specific adsorption capacities (Fig. 5D), which were comparable to the results of previous reports (Kong et al., 2015; Lv et al., 2018; Pasinszki et al., 2020; Wu et al., 2018). This suggests that an on-site supply of the Fe–FeS by plug-in modulation may be a viable option for customized adsorption of the HM^+ . Furthermore, dispersing Fe–FeS@G nanocomposites in HM^+ -containing solution instead of the base Fe–FeS clearly increased the adsorption capacity (Fig. 5D). The significant enhancement in HM^+ adsorption after incorporating G into Fe–FeS can be attributed to the increases in porosity. The obtained textural results using a porosimeter proved the significant increases in surface area (Fig. S6A) and pore volume (Fig. S6B) after the G incorporation, where type IV adsorption-desorption isotherms with a type H2 hysteresis loop for Fe–FeS@G matched the enhanced mesoporous structures (Hou et al., 2018). The resulting textural characteristics can be ascribed to covering of voids in the entangled Fe–FeS by the G nanosheets, which generates

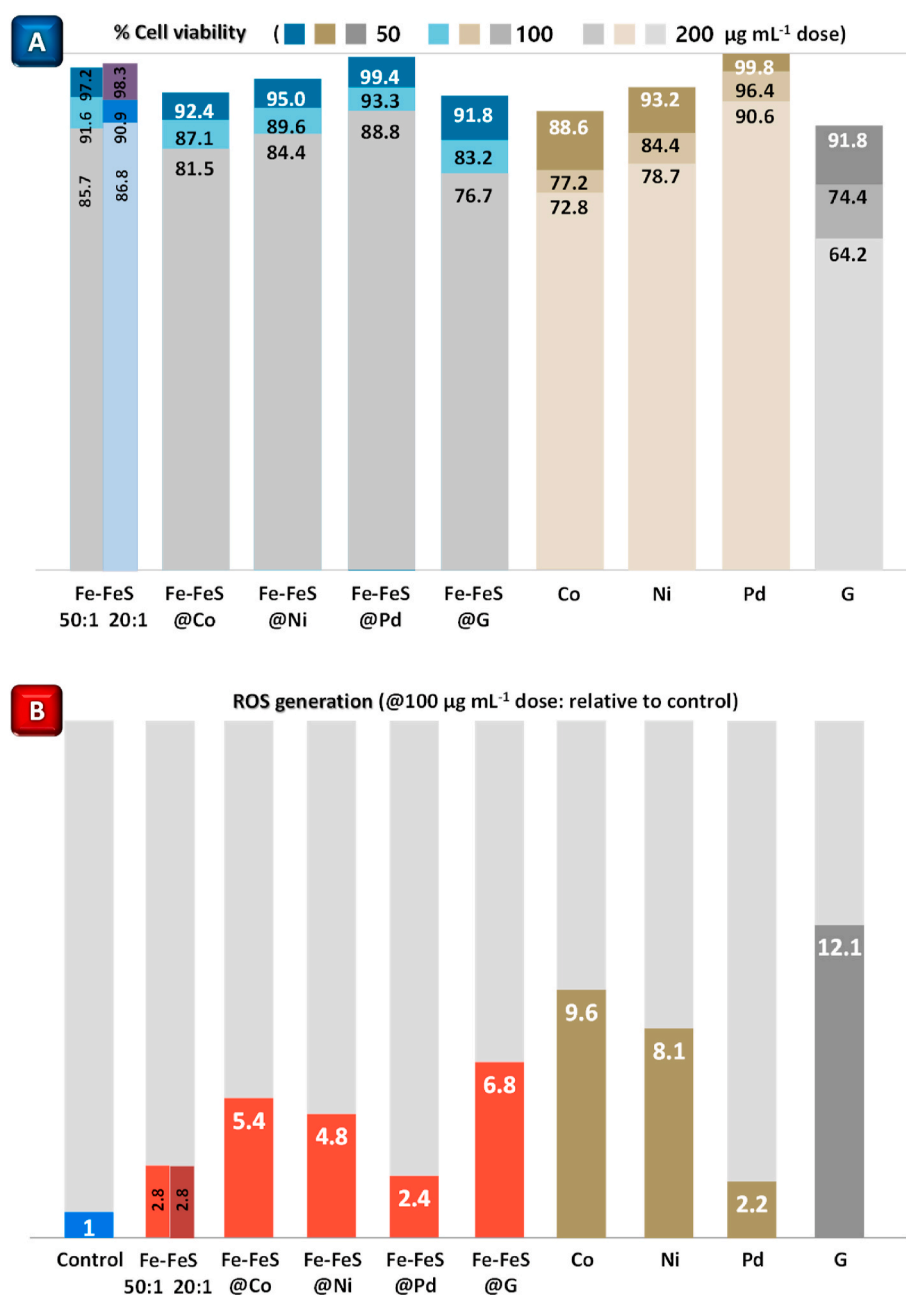


Fig. 6. Fundamental *in vitro* assays of Fe–FeS@Co, Fe–FeS@Ni, Fe–FeS@Pd, and Fe–FeS@G, including base Fe–FeS (Fe:S = 50:1 and 20:1) and individual Co, Ni, Pd, and G. (A) Cytotoxicity of the samples (incubation = 48 h) in HDF cells at different exposure concentrations (50–200 µg mL⁻¹; relevant to the sample concentrations in the effluent water from the membrane reactor). (B) Relative levels of ROS generation in HDF cells (incubation = 48 h) upon the exposure to a sample concentration of 100 µg mL⁻¹. The statistical significance (*p*) values of these tests were lower than 0.05.

additional mesoporous spaces. Whereas, base Fe–FeS exhibited an H4 hysteresis loop that is generally observed for complex structured materials containing limited micropores and mesopores (Thommes, 2010), suggesting that G layering may be another viable option for improving the adsorption capacity of complex structured Fe–FeS.

3.5. Cytotoxicity and ROS generation

The toxicity of base Fe–FeS and the effects of M or G incorporation on the toxicity were determined through *in vitro* assays. MTT assays of HDF (Fig. 6A) and BEAS-2B (Fig. S7A) cells after treatments with base Fe–FeS and their composites, including individual M NPs and G nanosheets exhibited dose-dependent characteristics at 50–200 $\mu\text{g mL}^{-1}$. The exposure concentrations were selected based on residual concentrations of the materials in the effluent water from TCE or HM^+ removal. Different levels of free radical and/or ROS generation in the cells caused by treatment with different architectures may induce differences in the cell viability (Henson et al., 2019). BEAS-2B exhibited rather sensitive responses to the exposures compared to dermal cells, representing better tolerance of dermal cells to the tested samples compared to the epithelial cells. The slightly lower viabilities were observed in both cell lines after incubation with the different composites (i.e., Fe–FeS@M and Fe–FeS@G) compared to those of the base Fe–FeS, which may be attributed to surficial arrangement of more toxic individual M NPs and G nanosheets, except in case of Fe–FeS@Pd. The decoration of Pd NPs with high biocompatibility reduced the toxicity of the base Fe–FeS (Rubio-Ruiz et al., 2018), which suggests that adding M NPs can also modulate the cytotoxicity of the base Fe–FeS. In DCFH-DA assays, relative levels of ROS (related to oxidative stresses inducing irreversible damages of lipids, proteins, and DNA) in both cell lines (Figs. 6B and S7B) treated with the different configurations (100 $\mu\text{g mL}^{-1}$) likely reflected the MTT assay results even for the cell-dependent sensitivities. This indicates that differing the cell lines for the exposures may cause different cytotoxic pathways that affects the levels of toxicity and ROS production. This suggests that potential adverse effects on human health and the environment caused by the exposure to water purifying materials require assessment of the matter from various angles, such as materials functionality and bio- and environmental safety. Therefore, developing a plug-in platform for on-site reconfiguration of the architectures of water purifying materials may offer various innovative strategies for effective and smart water purification based on AI, achieving modulable manufacturing, high purification performance, as well as bio- and environmental safety.

4. Conclusions

Unlike previously proposed water purification approaches that either focused on artificial intelligent (AI) planning of water treatment systems or automated supply of existing adsorbents and chemicals, in this study, plug-in devices were combined to achieve reconfigurable fabrication of water purifying materials (iron-iron sulfide [Fe–FeS], Fe–FeS@metal [M], and Fe–FeS@graphene [G]) with modulating removal of trichloroethylene (TCE) or heavy metal (lead, mercury, cadmium, and arsenic) ions (HM^+) in simulated contaminated water to offer realizable opportunities for smart water purification. Nanoscale Fe–FeS with different Fe:S ratios (10:1 to 90:1) was conveniently achieved through in-flight thiolation of photoionized Fe NPs (positively charged) by modulating thiol (negatively charged) content (10^{-3} to 10^{-1} v/v%) to determine the optimal Fe:S ratio for the TCE removal. In this system, spark ablation (Fe), droplet generation (thiol), and photo-irradiation (185-nm ultraviolet ray) were connected in series for a continued dispensing of Fe–FeS into the simulated contaminated water as well as generation of aqueous and solid wastes without any interruption to the process. The removal performance was enhanced by the incorporation of M nanocatalysts used for hydrogenation (cobalt, nickel, or palladium generated by another spark ablation) with Fe–FeS (50:1,

Fe:S) to facilitate the retardation of Fe corrosion during the TCE removal (Fe–FeS@Pd [0.221 h^{-1}] > Fe–FeS@Ni [0.184 h^{-1}] > Fe–FeS@Co [0.135 h^{-1}] vs. Fe–FeS [0.108 h^{-1}]). By selecting a different operation mode, the plug-in system enabled in-flight incorporation between Fe–FeS (Fe:S = 20:1) and G (from collision-type atomization) to provide enhanced HM^+ removal (Fe–FeS@G [299–592 mg g^{-1}] vs. Fe–FeS [106–196 mg g^{-1}]). *In vitro* toxicological profiles of the nanocomposites (Fe–FeS@M and Fe–FeS@G) exhibited slightly higher cytotoxicity and reactive oxygen species generation compared to Fe–FeS alone but lower values compared to individual M or G. The reconfigurable plug-in fabrication of Fe–FeS and its composites may provide adaptable platforms for AI planning-based water purification and offer conceptual insights on built-to-order fabrication of water purifying composite nanomaterials. Furthermore, the reconfigurable fabrication of composite nanostructures might be extended to construct other composite nanocatalysts for energy conversion and other environmental remediation processes, although combined operations of an AI platform and plug-in devices for exploratory researches on smart autonomous water purification should be sufficiently preceded.

Funding sources

This work was supported by the National Research Foundation of Korea (NRF) Grant funded by the Korean Government (MSIP) (No. 2015R1A5A1037668 and 2019R1C1C1007840).

CRedit authorship contribution statement

Bongseop Kwak: Experiment, Formal analysis, Writing – original draft. **Jungwook Choi:** Conceptualization, Formal analysis, Writing – review & editing, Supervision, Conceptualization, Investigation, Formal analysis, Writing – original draft, Writing – review & editing, Data curation, Supervision. **Jiseok Lim:** Conceptualization, Formal analysis, Writing – review & editing, Supervision, Funding acquisition.

Declaration of competing interest

The authors declare that they have no known competing financial interests or personal relationships that could have appeared to influence the work reported in this paper.

Appendix B. Supplementary data

Supplementary data to this article can be found online at <https://doi.org/10.1016/j.jclepro.2021.128069>.

References

- Aani, S.A., Bonny, T., Hasan, S.W., Hilal, N., 2020. Can machine language and artificial intelligence revolutionize process automation for water treatment and desalination? *Desalination* 458, 84–96.
- Bian, T., Chu, Z., Klajn, R., 2020. The many ways to assemble nanoparticles using light. *Adv. Mater.* 32, 1905866.
- Byeon, J.H., 2016. Aerosol nanoencapsulation: single-pass floating self-assembly of biofunctional hybrid nanoplateforms. *ACS Appl. Mater. Interfaces* 8, 17757–17762.
- Byeon, J.H., Roberts, J.R., 2014. Photoionization of nanosized aerosol gold agglomerates and their deposition to form nanoscale islands on substrates. *Langmuir* 30, 8770–8775.
- Cao, Z., Song, H., Cao, B., Ma, J., Chen, X., Zhou, J., Ma, Z., 2017. Sheet-on-sheet chrysanthemum-like C/FeS microspheres synthesized by one-step solvothermal method for high-performance sodium-ion batteries. *J. Power Sources* 364, 208–214.
- Chandrasekaran, S., Yao, L., Deng, L., Bowen, C., Zhang, Y., Chen, S., Lin, Z., Peng, F., Zhang, P., 2019. Recent advances in metal sulfides: from controlled fabrication to electrocatalytic, photocatalytic and photoelectrochemical water splitting and beyond. *Chem. Soc. Rev.* 48, 4178–4280.
- Choudhury, P., Mondal, P., Majumdar, S., Saha, S., Sahoo, G.C., 2018. Preparation of ceramic ultrafiltration membrane using green synthesized CuO nanoparticles for chromium (VI) removal and optimization by response surface methodology. *J. Clean. Prod.* 203, 511–520.
- Coley, C.W., Thomas III, D.A., Lummiss, J.A.M., Jaworski, J.N., Breen, C.P., Schultz, V., Hart, T., Fishman, J.S., Rogers, L., Gao, H., Hicklin, R.W., Plehiers, P.P., Byington, J.,

- Piotti, J.S., Green, W.H., Hart, A.J., Jamison, T.F., Jensen, K.F., 2019. A robotic platform for flow synthesis of organic compounds informed by AI planning. *Science* 365, eaax1566.
- Cummins, D.R., Russell, H.B., Jasinski, J.B., Menon, M., Sunkara, M.K., 2013. Iron sulfide (FeS) nanotubes using sulfurization of hematite nanowires. *Nano Lett.* 13, 2423–2430.
- Curl, J.M., Nading, T., Hegger, K., Barhoumi, A., Smoczynski, M., 2019. Digital twins: the next generation of water treatment technology. *J. Am. Water Works Assoc.* 111, 44–50.
- Dong, H., Hou, K., Qiao, W., Cheng, Y., Zhang, L., Wang, B., Li, L., Wang, Y., Ning, Q., Zeng, G., 2019. Insights into enhanced removal of TCE utilizing sulfide-modified nanoscale zero-valent iron activated persulfate. *Chem. Eng. J.* 359, 1046–1055.
- Dong, H., Zhang, C., Deng, J., Jiang, Z., Zhang, L., Cheng, Y., Hou, K., Tang, L., Zeng, G., 2018. Factors influencing degradation of trichloroethylene by sulfide-modified nanoscale zero-valent iron in aqueous solution. *Water Res.* 135, 1–10.
- Dutta, A.K., Maji, S.K., Srivastava, D.N., Mondal, A., Biswas, P., Paul, P., Adhikary, B., 2012. Synthesis of FeS and FeSe nanoparticles from a single source precursor: a study of their photocatalytic activity, peroxidase-like behavior, and electrochemical sensing of H₂O₂. *ACS Appl. Mater. Interfaces* 4, 1919–1927.
- Egeberg, A., Block, T., Janka, O., Wenzel, O., Gerthsen, D., Pöttgen, R., Feldmann, C., 2019. Lithiumpyridinyl-driven synthesis of high-purity zero-valent iron nanoparticles and their use in follow-up reactions. *Small* 15, 1902321.
- Elkin, E.R., Harris, S.M., Su, A.L., Lash, L.H., Loch-Caruso, R., 2020. Placenta as a target of trichloroethylene toxicity. *Environ. Sci.: Processes Impacts* 22, 472–486.
- Fan, D., Johnson, G.O., Tratnyek, P.G., Johnson, R.L., 2016. Sulfidation of nano zerovalent iron (nZVI) for improved selectivity during in-situ chemical reduction. *Environ. Sci. Technol.* 50, 9558–9565.
- Fan, M., Hu, J., Cao, R., Ruan, W., Wei, X., 2018. A review on experimental design for pollutants removal in water treatment with the aid of artificial intelligence. *Chemosphere* 200, 330–343.
- Feng, J., Biskos, G., Schmidt-Ott, A., 2015. Toward industrial scale synthesis of ultrapure singlet nanoparticles with controllable sizes in a continuous gas-phase process. *Sci. Rep.* 5, 15788.
- Feng, J., Huang, L., Ludvigsson, L., Messing, M.E., Maissner, A., Biskos, G., Schmidt-Ott, A., 2016. General approach to the evolution of singlet nanoparticles from a rapidly quenched point source. *J. Phys. Chem. C* 120, 621–630.
- Gautam, M., Park, D.H., Park, S.J., Nam, K.S., Park, G.Y., Hwang, J., Yong, C.S., Kim, J. O., Byeon, J.H., 2019. Plug-in safe-by-design nanoinorganic antibacterials. *ACS Nano* 13, 12798–12809.
- Genchev, G., Erbe, A., 2016. Raman spectroscopy of mackinawite FeS in anodic iron sulfide corrosion products. *J. Electrochem. Soc.* 163, C333–C338.
- Gong, Y., Tang, J., Zhao, D., 2016. Application of iron sulfide particles for groundwater and soil remediation: a review. *Water Res.* 89, 309–320.
- Guo, H., Yao, Z., Yang, Z., Ma, X., Wang, J., Tang, C.Y., 2017. A one-step rapid assembly of thin film coating using green coordination complexes for enhanced removal of trace organic contaminants by membranes. *Environ. Sci. Technol.* 51, 12638–12643.
- Gu, Y., Wang, B., He, F., Bradley, M.J., Tratnyek, P.G., 2017. Mechanochemically sulfidated microscale zero valent iron: pathways, kinetics, mechanism, and efficiency of trichloroethylene dechlorination. *Environ. Sci. Technol.* 51, 12653–12662.
- Hartrampf, N., Saebi, A., Poskus, M., Gates, Z.P., Callahan, A.J., Cowfer, A.E., Hanna, S., Antilla, S., Schissel, C.K., Quartararo, A.J., Ye, X., Mijalis, A.J., Simon, M.D., Loas, A., Liu, S., Jessen, C., Nielsen, T.E., Pentelute, B.L., 2020. Synthesis of proteins by automated flow chemistry. *Science* 368, 980–987.
- Herman, D.A.J., Ferguson, P., Cheong, S., Hermans, I.F., Ruck, B.J., Allan, K.M., Prabhakar, S., Spencer, J.L., Lendrum, C.D., Tilley, R.D., 2011. Hot-injection synthesis of iron/iron oxide core/shell nanoparticles for T₂ contrast enhancement in magnetic resonance imaging. *Chem. Commun.* 47, 9221–9223.
- Henson, T.E., Navratilova, J., Tennant, A.H., Bradham, K.D., Rogers, K.R., Hughes, M.F., 2019. In vitro intestinal toxicity of copper oxide nanoparticles in rat and human cell models. *Nanotoxicology* 13, 95–811.
- He, Y., Peng, G., Jiang, Y., Zhao, M., Wang, X., Chen, M., Lin, S., 2020. Environmental hazard potential of nano-photocatalysts determined by nano-bio interactions and exposure conditions. *Small* 16, 1907690.
- Himly, M., Geppert, M., Hofer, S., Hofstätter, N., Horejs-Höck, J., Duschl, A., 2020. When would immunologists consider a nanomaterial to be safe? Recommendations for planning studies on nanosafety. *Small* 16, 1907483.
- Hou, B.-H., Wang, Y.-Y., Guo, J.-Z., Ning, Q.-L., Xi, X.-T., Pang, X.-L., Cao, A.-M., Wang, X., Zhang, J.-P., Wu, X.-L., 2018. Pseudocapacitance-boosted ultrafast Na storage in a pie-like FeS@C nanohybrid as an advanced anode material for sodium-ion full batteries. *Nanoscale* 10, 9218–9225.
- Jiang, S., Ladewig, B.P., 2020. Green synthesis of polymeric membranes: recent advances and future prospects. *Curr. Opin. Green Sustain. Chem.* 21, 1–8.
- Kim, E.-J., Kim, J.-H., Azad, A.-M., Chang, Y.-S., 2011. Facile synthesis and characterization of Fe/FeS nanoparticles for environmental applications. *ACS Appl. Mater. Interfaces* 3, 1457–1462.
- Kim, E.-J., Kim, J.-H., Chang, Y.-S., Turcio-Ortega, D., Tratnyek, P.G., 2014. Effects of metal ions on the reactivity and corrosion electrochemistry of Fe/FeS nanoparticles. *Environ. Sci. Technol.* 48, 4002–4011.
- Kim, E.-J., Murugesan, K., Kim, J.-H., Tratnyek, P.G., Chang, Y.-S., 2013. Remediation of trichloroethylene by FeS-coated iron nanoparticles in simulated and real groundwater: effects of water chemistry. *Ind. Eng. Chem. Res.* 52, 9343–9350.
- Kong, L., Yan, L., Qu, Z., Yan, N., Li, L., 2015. β -cyclodextrin stabilized magnetic Fe₃S₄ nanoparticles for efficient removal of Pb(II). *J. Mater. Chem. C* 3, 15755–15763.
- Lee, S.Y., Kang, Y.C., 2016. Sodium-ion storage properties of FeS-reduced graphene oxide composite powder with a crumpled structure. *Chem. Eur. J.* 22, 2769–2774.
- Li, R., Zhang, L., Wang, P., 2015. Rational design of nanomaterials for water treatment. *Nanoscale* 7, 17167–17194.
- Li, Z., Jia, Z., Ni, T., Li, S., 2017. Green and facile synthesis of fibrous Ag/cotton composites and their catalytic properties for 4-nitrophenol reduction. *Appl. Surf. Sci.* 426, 160–168.
- Lv, D., Zhou, X., Zhou, J., Liu, Y., Li, Y., Yang, K., Lou, Z., Baig, S.A., Wu, D., Xu, X., 2018. Design and characterization of sulfide-modified nanoscale zerovalent iron for cadmium(II) removal from aqueous solutions. *Appl. Surf. Sci.* 442, 114–123.
- Mahto, A., Kumar, A., Chaudhary, J.P., Bhatt, M., Sharma, A.K., Paul, P., Nataraj, S.K., Meena, R., 2018. Solvent-free production of nano-FeS anchored graphene from Ulva fasciata: a scalable synthesis of super-adsorbent for lead, chromium and dyes. *J. Hazard Mater.* 353, 190–203.
- Maji, S.K., Dutta, A.K., Biswas, P., Srivastava, D.N., Paul, P., Mondal, A., Adhikary, B., 2012. Synthesis and characterization of FeS nanoparticles obtained from a dithiocarboxylate precursor complex and their photocatalytic, electrocatalytic and biomimic peroxidase behavior. *Appl. Catal. A-Gen.* 419–420, 170–177.
- Ma, Y., Elankumaran, S., Marr, L.C., Vejerano, E.P., Pruden, A., 2014. Toxicity of engineered nanomaterials and their transformation products following wastewater treatment on A549 human lung epithelial cells. *Toxicol. Rep.* 1, 871–876.
- Mohamed, S.K., Abuelhamd, M., Allam, N.K., Shahat, A., Ramadan, M., Hassan, H.M.A., 2020. Eco-friendly facile synthesis of glucose-derived microporous carbon spheres electrodes with enhanced performance for water capacitive deionization. *Desalination* 477, 114278.
- Neogrady, P., Kello, V., Urban, M., Sadlej, A.J., 1997. Ionization potentials and electron affinities of Cu, Ag, and Au: electron correlation and relativistic effects. *Int. J. Quant. Chem.* 63, 557–565.
- Niu, S., Jiang, W.-J., Tang, T., Yuan, L.-P., Luo, H., Hu, J.-S., 2019. Autogenous growth of hierarchical NiFe(OH)x/FeS nanosheet-on-microsheet arrays for synergistically enhanced high-potential water oxidation. *Adv. Funct. Mater.* 29, 1902180.
- Parvez, S., Long, M.J.C., Poganik, J.R., Aye, Y., 2018. Redox signaling by reactive electrophiles and oxidants. *Chem. Rev.* 118, 8798–8888.
- Pasinski, T., Krebs, M., Chand, D., Kótai, L., Homonnay, Z., Sajó, I.E., Váci, T., 2020. Carbon microspheres decorated with iron sulfide nanoparticles for mercury(II) removal from water. *J. Mater. Sci.* 55, 1425–1435.
- Podgorski, J., Berg, M., 2020. Global threat of arsenic in groundwater. *Science* 368, 845–850.
- Poudel, B.K., Doh, K.-O., Byeon, J.H., 2018. Ag photoionization-induced single-pass assembly of Ag₂S nanodots in flowing thiol droplets. *Green Chem.* 20, 978–983.
- Poudel, B.K., Hwang, J., Ku, S.K., Kim, J.O., Byeon, J.H., 2019. Plug-and-play continuous flow assembly of cysteine-inserted AuCu nanobimetal for folate-receptor-targeted chemo-phototherapy. *ACS Appl. Mater. Interfaces* 11, 17193–17203.
- Ren, L., Li, L., Chen, S., Li, H., Liu, Y., Zhou, L., Guo, S., 2019. Yolk-shell Fe/FeS@SiO₂ particles with enhanced dispersibility, transportability and degradation of TBBPA. *Catal. Today* 327, 2–9.
- Rubio-Ruiz, B., Pérez-López, A.M., Bray, T.L., Lee, M., Serrels, A., Prieto, M., Arruebo, M., Carragher, N.O., Sebastián, V., Unciti-Broceta, A., 2018. High-precision photothermal ablation using biocompatible palladium nanoparticles and laser scanning microscopy. *ACS Appl. Mater. Interfaces* 10, 3341–3348.
- Santhosh, C., Velmurugan, V., Jacob, G., Jeong, S.K., Grace, A.N., Bhatnagar, A., 2016. Role of nanomaterials in water treatment applications: a review. *Chem. Eng. J.* 306, 1116–1137.
- Soori, M., Zarezadeh, K., Sheibani, S., Rashchi, F., 2016. Mechano-chemical processing and characterization of nano-structured FeS powder. *Adv. Powder Technol.* 27, 557–563.
- Sui, J., Yan, J., Liu, D., Wang, K., Luo, G., 2020. Continuous synthesis of nanocrystals via flow chemistry technology. *Small* 16, 1902828.
- Su, L., Liu, C., Liang, K., Chen, Y., Zhang, L., Li, X., Han, Z., Zhen, G., Chai, X., Sun, X., 2018. Performance evaluation of zero-valent iron nanoparticles (NZVI) for high-concentration H₂S removal from biogas at different temperatures. *RSC Adv.* 8, 13798–13805.
- Thapa, R.K., Ku, S.K., Choi, H.-G., Yong, C.S., Byeon, J.H., Kim, J.O., 2018. Vibrating droplet generation to assemble zwitterion-coated gold-graphene oxide stealth nanovesicles for effective pancreatic cancer chemo-phototherapy. *Nanoscale* 10, 1742–1749.
- Thommes, M., 2010. Physical adsorption characterization of nanoporous materials. *Chem. Ing. Tech.* 82, 1059–1073.
- Verma, P., Samanta, S.K., 2018. Continuous ultrasonic stimulation based direct green synthesis of pure anatase-TiO₂ nanoparticles with better separability and reusability for photocatalytic water decontamination. *Mater. Res. Express* 5, 065049.
- Wang, L., Zhao, Y., Tian, Y., 2015. Two-dimensional FeS nanoflakes: synthesis and application to electrochemical sensor for mercury(II) ions. *J. Nano Res.* 17, 393.
- Wang, S., Liu, Z., Wang, W., You, H., 2017. Fate and transformation of nanoparticles (NPs) in municipal wastewater treatment systems and effects of NPs on the biological treatment of wastewater: a review. *RSC Adv.* 7, 37065–37075.
- Wang, Y., O'Connor, D., Shen, Z., Lo, I.M.C., Tsang, D.C.W., Pehkonen, S., Pu, S., Hou, D., 2019. Green synthesis of nanoparticles for the remediation of contaminated waters and soils: constituents, synthesizing methods, and influencing factors. *J. Clean. Prod.* 226, 540–549.
- Wu, D., Peng, S., Yan, K., Shao, B., Feng, Y., Zhang, Y., 2018. Enhanced As(III) sequestration using sulfide-modified nano-scale zero-valent iron with a characteristic core-shell structure: sulfidation and as distribution. *ACS Sustain. Chem. Eng.* 6, 3039–3048.
- Wu, Z., Shi, P., Lim, H.K., Ma, Y., Setyawati, M.I., Bitounis, D., Demokritou, P., Ng, K.W., Tay, C.Y., 2020. Inflammation increases susceptibility of human small airway epithelial cells to pneumonic nanotoxicity. *Small* 16, 2000963.

- Xin-yan, Z., Ting-ting, T., Yao, W., Jing-yue, Y., Xue, W., Yan-yan, G., Qun, S., Xin, Z., Shao-qing, Z., 2019. Green synthesis of Cu-SSZ-13 zeolite by seed-assisted route for effective reduction of nitric oxide. *J. Clean. Prod.* 236, 117667.
- Xu, J., Avellan, A., Li, H., Liu, X., Noël, V., Lou, Z., Wang, Y., Kaegi, R., Henkelman, G., Lowry, G.V., 2020. Sulfur loading and speciation control the hydrophobicity, electron transfer, reactivity, and selectivity of sulfidized nanoscale zerovalent iron. *Adv. Mater.* 32, 1906910.
- Xu, J., Tang, J., Baig, S.A., Lv, X., Xu, X., 2013. Enhanced dechlorination of 2,4-dichlorophenol by Pd/Fe-Fe₃O₄ nanocomposites. *J. Hazard Mater.* 244–245, 628–636.
- Ye, Z., Yang, J., Zhong, N., Tu, X., Jia, J., Wang, J., 2020. Tackling environment challenges in pollution controls using artificial intelligence: a review. *Sci. Total Environ.* 699, 134279.
- Yin, Z., Cui, C., Chen, H., Duoni, Yu, X., Qian, W., 2020. The application of carbon nanotube/graphene-based nanomaterials in wastewater treatment. *Small* 16, 1902301.
- Zhang, Q., Yao, X., Mwizerwa, J.P., Huang, N., Wan, H., Huang, Z., Xu, X., 2018. FeS nanosheets as positive electrodes for all-solid-state lithium batteries. *Solid State Ionics* 318, 60–64.
- Zhang, W.-x., Wang, C.-B., Lien, H.-L., 1998. Treatment of chlorinated organic contaminants with nanoscale bimetallic particles. *Catal. Today* 40, 387–395.
- Zhang, Y., Luo, K., Yu, J., Jiang, X., 2019. Green fabrication of SH-modified GO composite for heavy metal ions removal in aqueous solution. *Micro & Nano Lett.* 14, 373–378.
- Zhang, Y., Wu, B., Xu, H., Liu, H., Wang, M., He, Y., Pan, B., 2016. Nanomaterials-enabled water and wastewater treatment. *NanoImpact* 3–4, 22–39.
- Zhao, C., Shao, X., Zhu, Z., Zhao, C., Qian, X., 2017. One-pot hydrothermal synthesis of RGO/FeS composite on Fe foil for high performance supercapacitors. *Electrochim. Acta* 246, 497–506.
- Zhao, L., Dai, T., Qiao, Z., Sun, P., Hao, J., Yang, Y., 2020. Application of artificial intelligence to wastewater treatment: a bibliometric analysis and systematic review of technology, economy, management, and wastewater reuse. *Process Saf. Environ.* 133, 169–182.